Efficient dike monitoring using terrestrial SFM photogrammetry

L. Froideval, Christophe Conessa, Xavier Pellerin Le Bas, Laurent Benoît, Dominique Mouazé

▶ **To cite this version:**

EFFICIENT DIKE MONITORING USING TERRESTRIAL SFM PHOTOGRAMMETRY

L. Froideval[1*], C. Conessa[1], X. Pellerin Le Bas[2], L. Benoit[1], D. Mouazé[1]

[1] Normandie Univ, UNICAEN, UNIROUEN, CNRS, M2C, 14000 Caen, France -
(laurent.froideval, christophe.conessa, laurent.benoit, dominique.mouaze)@unicaen.fr
[2] Scienteama, 14610 Villons les Buissons, France - xavier.pellerin@scienteama.fr

Commission II, WG II/10

KEY WORDS: SFM, photogrammetry, dike, monitoring, point cloud, 3D time series.

ABSTRACT:

Nature based solutions are growing rapidly in order to mitigate in the near future the effects of climate change and rise of sea level on most anthropogenic coasts. In that frame, the CHERbourg bLOC (CHERLOC) project aims to study new coastal engineering solutions (overtopping, sediment transport) thanks to two new artificial units in two test sites (Normandy, France) considering biodiversity preservation but also societal acceptability. This study details an efficient method to monitor such coastal infrastructure using terrestrial Structure from Motion (SfM). In 2021, surveys were conducted to acquire pictures in April, May, June and November. A time series of 3D photogrammetric models was generated using open source SfM software. The first model was georeferenced using Ground Control Points (GCP) measured by Differential Global Navigation Satellite System (DGNSS) so that it could be used as a reference for the following point clouds using surrounding ripraps assumed to be non-mobile through the period of the study. The georeferencing Root Mean Square Error (RMSE) was found to be 1.8 cm for the April model whereas RMSEs of relative registrations of the following dates were found to be sub-centimetric. These results can be used to observe and measure blocks displacements as well as sand volumes evolution throughout the time series. The biggest displacement was found to be 23 cm between April and June. Sand topographic variation shows a continuous accumulation on selected cross-sections between April and November with an overall height accumulation of about 30 cm. Sand volumes measurements show consistent results with an added volume of 3.67 m^3 on the previous areas.

1. INTRODUCTION

Structure from Motion (SfM) photogrammetry is now widely used in geomorphology as demonstrated in Eltner et al. (2016) and Zekkos et al. (2018) has shown it to be accurate enough to be used for geotechnical applications. Oats et al. (2019) showed that SfM is suitable for displacements measurements. It is thus suited for coastal infrastructure applications as illustrated for instance by Guillot et al. (2015).

Most studies focus on Unmanned Aerial Vehicle (UAV) photogrammetry such as Tournade et al. (2014), Brauneck et al. (2016) or Hastaoğlu et al. (2019) in order to monitor breakwaters. Recent work of Zhou et al. (2019) even focuses on automatic metrology with UAV photogrammetry for such application.

Bakula et al. (2016) and Bakula et al. (2020) investigated the use of coupled photogrammetric and topographic Light Detection And Ranging (LiDAR) data in order to survey damages on dikes. Bakula et al. (2018) showed a comprehensive dike monitoring system using multi-sourced remote sensing data. Antoine et al. (2019) presented another dike focused multi-sensor UAV including LiDAR, thermal infrared, near-infrared and visible sensors used to detect a large number of surface indicators for pluri-kilometric dikes.

However, few studies focus on smaller dikes. According to Dering et al. (2019), at a lower scale, terrestrial SfM is more suitable than UAV photogrammetry. For instance, it is more

convenient with less field constraints such as wind conditions. In this study, we present an efficient method to monitor the main armour dike's deformation by terrestrial SfM photogrammetry. A 3D model times series on a *in situ* test dike is obtained by registering the different dates onto the first date in a robust manner. This limits the use of Ground Control Points (GCP) during the surveys and, in turn, saves useful time during pictures acquisitions that are constrained by tidal conditions.

2. THE CHERLOC PROJECT

2.1 A novel dike design

The goal of the CHERbourg bLOC (CHERLOC) project is to test two new kinds of blocks (concrete artificial units) for coastal protection. Although natural solutions are now encouraged, protective infrastructure is still necessary. The new design aims at improving the defence efficiency by increasing the stability and limiting overtopping phenomenon. In addition, it helps stimulate the interaction between the blocks and the biodiversity. The two blocks in Figure 1 are: a double-cube, designed by the laboratory of Continental and Coastal Morphodynamics (M2C) in Normandy, France that will be used as the main armour and an Accroberm^{TM} II, designed by Artelia that will serve as the toe (foot base). Its hollow shape design will both reduce the environmental footprint and increase biodiversity by developing new habitats opportunities while increasing the toe stability. The CHERLOC project serves as a test project for these blocks. Accurate and regular displacements

---

* Corresponding author

measurements is thus mandatory to validate this new kind of engineering solution. The dike stability depends on surface contact that should not be higher than a few centimetres for such concrete blocks. Kaidi et al. (2012) showed that numerical models predict damages for displacements of 15 cm or more.

2.2 Study sites

In this project, two test sites were chosen that are located in Normandy, France in the city of Cherbourg and Ouistreham. This paper will focus mostly on the latter as construction work on the first site was only recently achieved.

Figure 1. A: Accroberm™ II (2.24 m diameter); B: 'double cube' unit (1.3 m nominal diameter)

This new experimental dike was installed in March 2021 in the city of Ouistreham, France, at the end of the Riva Bella beach, close to the Ferry terminal. The overall shape is a rectangle of 30 m long and 15 m wide. It is composed of Accroberms™ II on the outside and blocks on the inside as shown on Figure 2.

Figure 2. Test dike in Ouistreham

3. METHOD

3.1 Data acquisition

The last block of the dike was installed in March 2021. Four photogrammetric field surveys were conducted in March, April, June and November 2021. Pictures acquisition were constrained to low tides and overcast conditions were chosen to minimize shadows, following Gienko and Terry (2014).

3.2 Equipment

Pictures were taken with a camera mounted on a three-meter fishing rod and triggered remotely using the dedicated tablet

application, allowing of real time coverage checks as seen on Figure 3.

Figure 3. Pole data acquisition

Two different camera models were used depending on the date, and fixed focal lenses were chosen to improve picture quality and reduce the risk of focal length changes during the survey. The first camera was a Digital Single-Lens Reflex (DSLR) Cannon EOS 80D with a focal length of 18 mm. The second camera was a mirrorless Sony A6000 with a focal length of 16 mm. Both cameras have APS-C sensor size and can capture pictures with a 6000 pixel by 4000 pixel resolution. A summary of the cameras used along with the number of pictures taken per date can be found in Table 1.

3D Model	Date 2021	Camera Model	Focal Length [mm]	Aperture
1	April 28	Canon EOS 80D	18	F/11 to F/9
2	May 11	Canon EOS 80D	18	F/22
3	June 30	Canon EOS 80D	18	F/18 to F/16
4	November 3	Sony A6000	16	F/8 to F/5.6

Table 1. Technical data of used cameras

3.3 Picture patterns

Picture acquisition patterns as seen on Figure 4 was established to ensure a good coverage with substantial overlaps as well as maximizing the angle of parallax to ensure a good reconstruction. More specifically, pictures were taken with the camera mounted on the three-meter fishing rod every three steps and going around the whole structure twice, changing the angle of the camera for each round. In addition, pictures were acquired on foot every three steps, going around the structure twice again, at two different distances of about 1 and 3 meters.
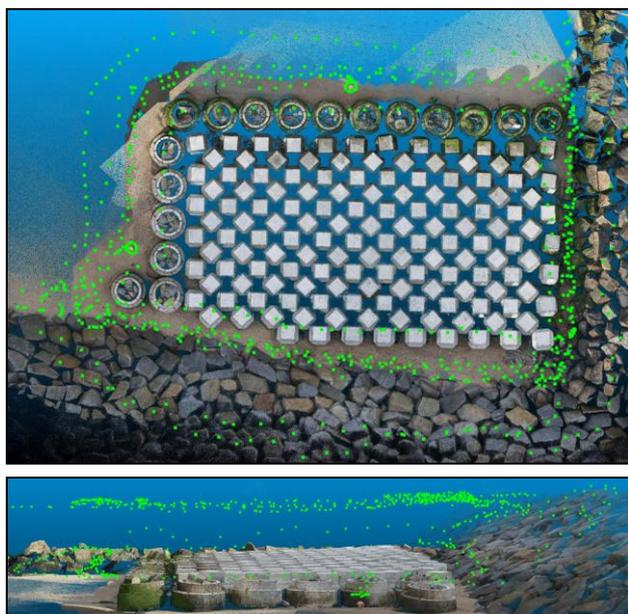
Figure 4. Picture acquisition pattern

3.4 GCPs

Two surveys made use of GCPs based on targets: the first date for georeferencing and the second one to be used as control points. Overall, ten targets, represented on Figure 5, were set on the field, around the structure while performing the survey: 8 flat targets as well as two spherical targets of known diameter that will help in the accuracy assessment.

The spherical shape insures a more robust identification than a ruler as in Froideval et al. (2019). Randomly speckled hollow concrete spheres were chosen to be carried easily on the field and sustain weather conditions. All these targets were surveyed using Differential Global Navigation Satellite System (DGNSS).

Figure 5. Spherical (on the left) and flat (on the right) targets

3.5 3D models generation

Photogrammetric dense point clouds were generated using OpenMVG (Moulon et al., 2016) with Scale-Invariant Feature Transform (SIFT) descriptors (Lowe, 2004) to compute the features for each picture. The camera is modelled by the classic pinhole model using the focal, principal point, image size as well as the radial distortion. Overlaps are then found by establishing the corresponding putative photometric matches. Results are then processed with robust geometric filters. For pictures orientation, a sequential SfM method is then applied based on Moulon, et al. (2012). It is a growing reconstruction

process starting with an initial pair of pictures. Lastly, OpenMVS (OpenMVS, 2018) is used for densification as in Froideval et al. (2019). Table 2 indicates the number of pictures taken, the number of pictures properly oriented, the number of points generated for each date as well as the Root Mean Square Error (RMSE) of the picture orientation accuracy in pixel. It is interesting to notice that the higher the number of pictures oriented is, the lower the error gets. Due to the very high number of points generated, computed point clouds were then subsampled to 30 million points, resulting in an average surface point density represented on Figure 6 that ranges from 20 to 60 x 10^3 pts/m^2 on the dike structure and on the sand.

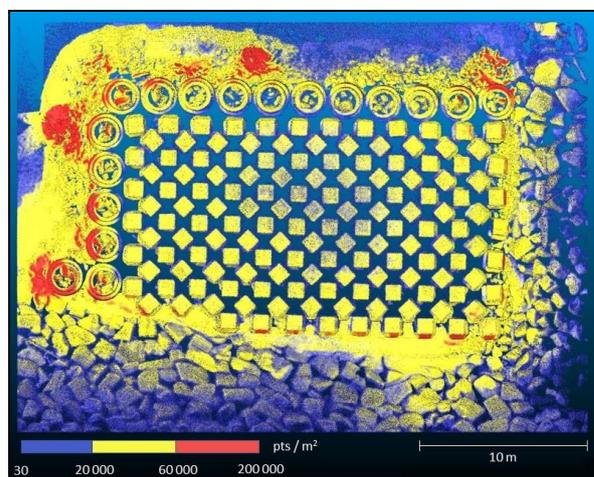| Date	Number of pictures oriented / taken	Number of points [million]	RMSE [pixel]
April	557 / 557	391	0.77
May	561 / 566	372	0.78
June	646 / 646	471	0.70
November	722 / 722	431	0.57

Table 2. Photogrammetric models

Figure 6. Surface point cloud density in April

3.6 Registration

For this study, the first model was georeferenced using DGNSS and the following models were in turn registered relatively to the first model using the non-mobile riprap surrounding the structure.
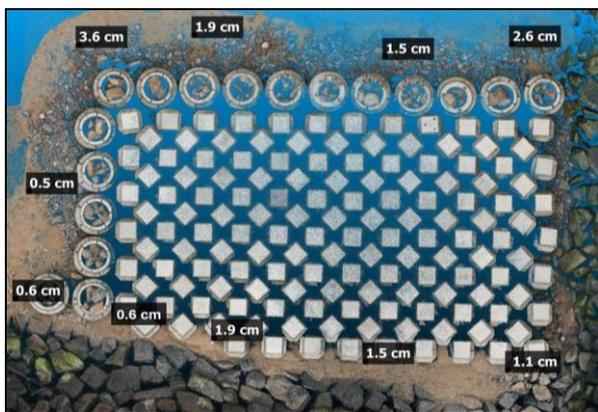
Figure 7. Georeferencing errors on each of the ten targets

Georeferencing of the first model was made using the ten targets surveyed with DGNSS as illustrated on Figure 7. The computation was made using CloudCompare (Girardeau-Montaut, 2011) and the RMSE was found to be 1.8 cm. Registration of model 2 onto model 1 was made in two steps in a coarse, or manual registration, followed by a fine registration. For the first step, four sets of five points spread homogeneously were chosen on the riprap surrounding the structure. The average point density on this area was found to be around 20×10^3 pts/m^2. These rocks are assumed to be perfectly stable throughout the whole study. Then, the fine registration was made using the iterative closest point algorithm implementation in CloudCompare (Besl and McKay, 1992) on the riprap. Allowing a scale adjustment, the RMSE difference between two iterations was set to 1×10^{-5} m with no further point cloud subsampling. A final overlap of 100% was asked. Table 3 summarizes the RMSE of the coarse and fine registration for the different models. For the first date, the RMSE of the coarse registration represents the georeferencing error. These differences were computed using 5 million points. The registration results are here below 1 cm, meaning displacements above 1 cm can be considered significant.

Date	RMSE Coarse Registration [cm]	RMSE Fine Registration [cm]
April	1.8	-
May	2.2	0.7
June	1.2	0.9
November	0.7	0.8

Table 3. Root mean square error of the registration steps

3.7 Accuracy assessment

To check the registration, differences between April and May, May and June, June and November as well as May and November were computed on the riprap. RMSEs were computed using the mean and standard deviation of the differences obtained with CloudCompare using a local quadric modelling. Results of these comparisons can be seen on Table 4 and are sub-centimetric.

Additional steps were taken to check the registration process. First, DGNSS measurements of the ten targets on date 2 were compared to their coordinates in the model already registered with date 1 with a computed mean error of 1.25 cm and a standard deviation of 0.7 cm.

Dates	RMSE [cm]
May - April	0.7
June - May	0.4
November - June	0.7
May-November	0.6

Table 4. Error between the different dates

Then, for each survey, the radius of the two modelled spherical targets were compared to the actual radius of the target placed on the field close to the structure. To measure the radius in the model, automatic identification was made using the random sample consensus (RANSAC) algorithm (Schnabel et al., 2007). Mean error between the modelled spherical targets and the actual ones is of 2.15% for April and May, 2.05% for June and 2.35% for November. Detailed results per target can be found on Table 5.

Target	Radius modelled [cm]	Radius theoretical [cm]	Error [cm]	Error [%]
April (1)	12.7	12.5	0.2	1.6
April (2)	15.4	15	0.4	2.7
May (1)	12.7	12.5	0.2	1.6
May (2)	15.4	15	0.4	2.7
June (1)	12.6	12.5	0.1	0.8
June (2)	15.5	15	0.5	3.3
November (1)	15.5	15	0.5	3.1
November (2)	14.8	15	0.2	1.6

Table 5. 3D spherical target errors

3.8 Differences

To compute the displacements more easily, point clouds were subsampled to 3 million points corresponding to point density of more than 5×10^3 pts/m^2.

Point cloud normals were computed using CloudCompare with a quadric local model suited for curvy surfaces and the suggested best fit neighbourhood size. The normal orientations were computed with a +Z preference, insuring a better consistency.

Differences between the first and the last date were computed using M3C2 algorithm in CloudCompare (Lague et al., 2013). The full 3 million points were used as well as previously computed normals, depth of 1 m and automatically computed cylinder diameter.

4. RESULTS

4.1 Time series evolution

Overall differences between the first survey date, April, and the last one on November are shown on Figure 8. Although most areas do not present significant changes, some blocks displacements as well as sand movement are noticeable. More details about the scene evolution can be seen on Figure 9, 10 and 11 showing differences between April and May, May and June as well as June and November.
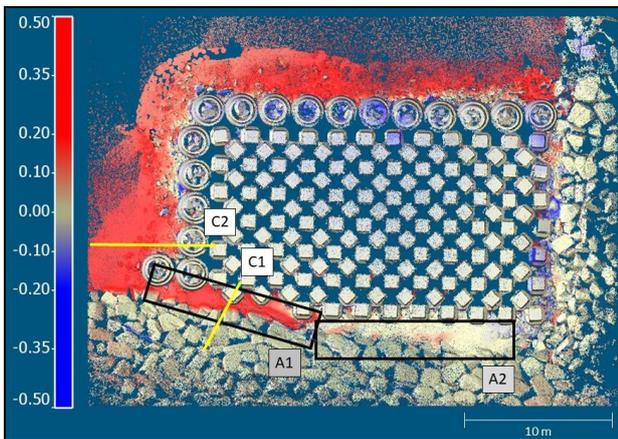
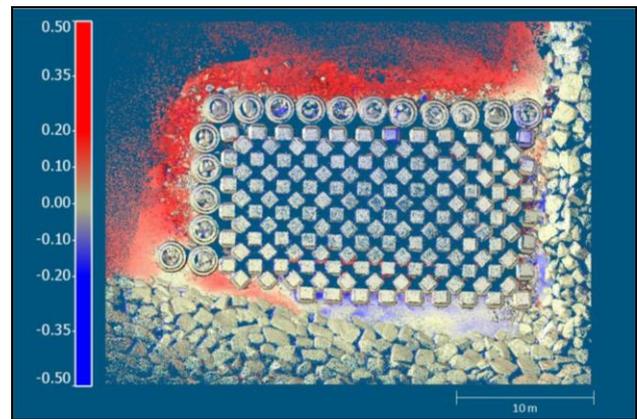**Figure 8.** April / November differences [m]

Figure 9. April / May differences [m]

Figure 10. May / June differences [m]

Figure 11. June / November differences [m]
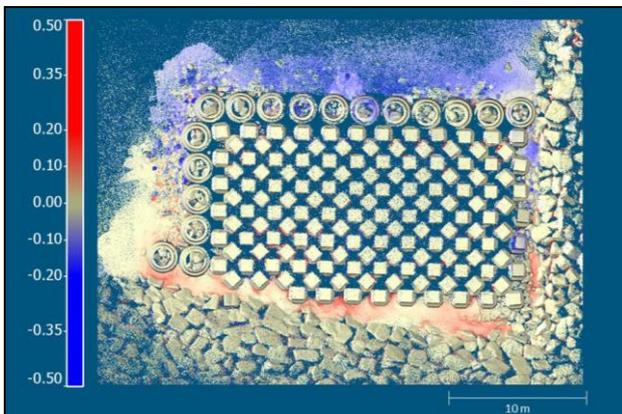
4.2 Blocks displacements

We can take a closer look at the displacements of the blocks with the 3D model time series as shown on Figure 12 where the block on the left represents the South-East corner of the structure. Here, and for the following examples, dates are colour coded as follows: green for April, yellow for May, blue for June and red for November. We first notice that the left block did not move between April and November whereas the other two show visible displacements between May and June.
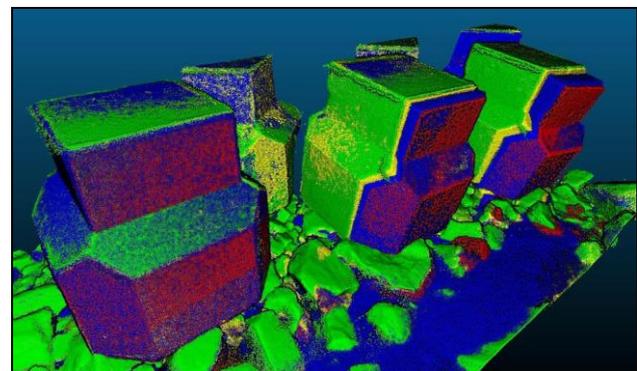

Figure 12. Close view of the displacements

Using the point cloud of differences previously computed between April and November, we measure a displacement (overturning mainly and slight settlement) of 16 cm for the middle block and 23 cm for the block on the far right. Figure 13 shows a cross-section of this block with consistent displacements on both sides. We notice here again that the biggest change is observed between April and June.

Figure 13. Cross-section view of the displacements [m]

4.3 Sand topographic variation

4.3.1 Cross-section

To observe the evolution of sand topography, we show here two examples with cross-section C1 and C2 taken on the South-West corner of the structure as shown on Figure 8. On Figure 14, we see the sand accumulation between the block and the riprap over time through the 3D model time series. Over time, we see a continuous accumulation from April to November (low wave energy period) with sand filling wholes while flattening the surface. The overall height accumulation can be measured and is of the order of 30 cm. It is also interesting to note that both the blocks on the left and the rocks on the right side do not show any significant displacement.
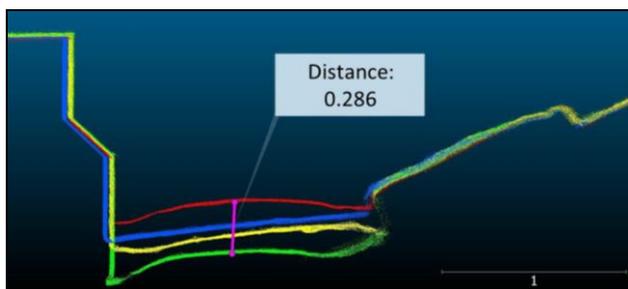

Figure 14. Topographic variations for cross-section C1

The second example is shown with cross-section C2 represented on Figure 15. In this area, sand tends to accumulate as well through the time series. The overall difference between the first and the last date is again around 30 cm as show on Figure 16. We notice on the side view of the cross-section on Figure 17 that the nearby Accroberm™ II does not show significant changes.
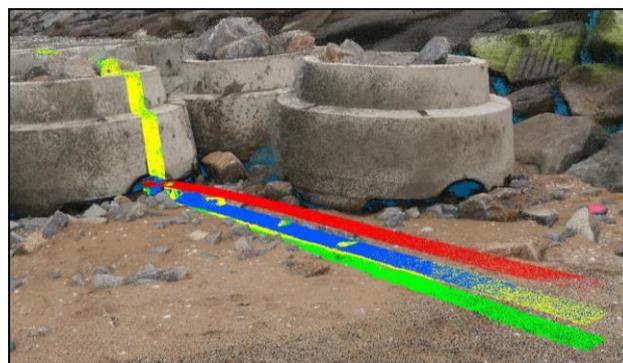

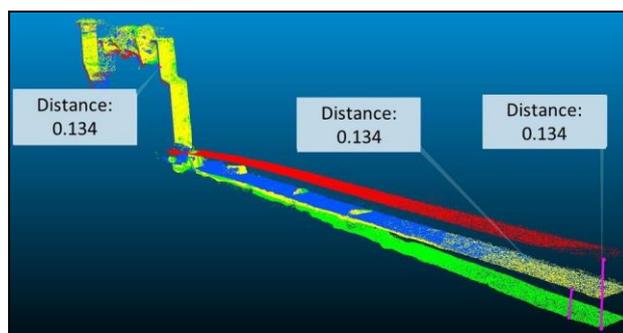**Figure 15**. Close view of the topographic variations for C2

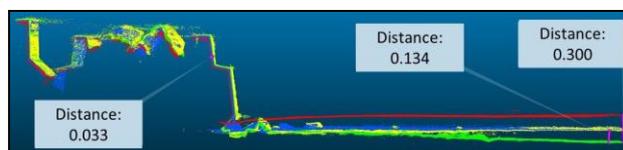**Figure 16**. Close view of the topographic variations [m]

Figure 17. Close view of the topographic variations [m]

4.3.2 Volumes

Furthermore, sand volumes can be computed using the time series. As an example, we computed volumes differences on area A1, shown on Figure 8 between April and November. Point density is here of about 50×10^3 pts/m². Using CloudCompare, both point clouds were rasterized with a 1 cm grid step and millimetric numerical precision. Results show an added sand volume of about 3.67 m³. Using the computed surface and the registration error, we obtain an uncertainty of 0.28 m³. This is consistent with Figure 8. Indeed, the size of area A1 is of about 10 m by 1 m and would thus results in an order of magnitude of the heights difference of about 30 cm. As a comparison, we then looked at area A2 where point clouds differences show little differences. Similar sand volume computation gives +0.16 m³ with an uncertainty of about 0.13 m³, meaning there is only a 0.03 m³ significant sand volume added which is very small compared to the surface area of 16.71 m².

5. DISCUSSION

The registration process of date 2, 3 and 4 on date 1 gives results of less than 1 cm in RMSE and is very robust with 5 million points used. This allows the use of targets measured by DGNSS only for the first date, which is more efficient than

using targets for every surveys. This will in turn simplify the survey process by saving time, crucial with tidal constraints.

As we saw in this study, centimetric registration is enough to observe displacements higher than the few centimetres required for monitoring such blocks but can also be used to analyse fine sand surfacic and volumic changes that can potentially be the cause of some of the dike's rearrangement.

Considering the blocks, results show the biggest change between April and June. One possible reason would be frequent strong winds in the North-East direction at this period of time in the local vicinity of Ouistreham but also an initial deficit of rock basement and the peripheral unit position, lacking contacts with neighbour units and hence decreasing stability.

A similar method is applied on the second CHERLOC site in Cherbourg. The blocks and Accroberm™ II were installed on both sides of the East part of the existing harbour's dike. For now, only one survey was made with 351 pictures resulting in a 211 million points photogrammetric model with a reconstruction RMSE of 0.73 pixel. An illustration of the model can be seen on Figure 18.
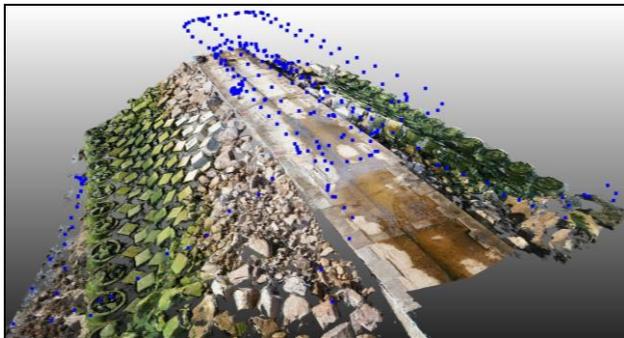
Figure 18. Photogrammetric model of the dike in Cherbourg

Photogrammetric surveys on the CHERLOC projects will still be ongoing in 2022 on both sites. It will be interesting to analyse the displacements after the seasonal winter storms in those areas.

ACKNOWLEDGEMENTS

REFERENCES

Antoine, R., Tanguy, M., Palma Lopes, S., Sorin, J.-L., 2019. Didro-An Innovative Multi-Sensor UAV System for Routine and Crisis Monitoring of Dikes, in: *AGU Fall Meeting Abstracts*. pp. EP11C-2123. Bibcode: 2019AGUFMEP11C2123A

Bakula, K., Ostrowski, W., Szender, M., Plutecki, W., Salach, A., Górski, K., 2016. POSSIBILITIES FOR USING LIDAR AND PHOTOGRAMMETRIC DATA OBTAINED WITH AN UNMANNED AERIAL VEHICLE FOR LEVEE MONITORING. *International Archives of the Photogrammetry,*

Remote Sensing & Spatial Information Sciences 41. https://doi.org/10.5194/isprs-archives-XLI-B1-773-2016

Bakula, K., Zelaya Wziątek, D., Weintrit, B., Jędryka, M., Ryfa, T., Pilarska, M., Kurczyński, Z., 2018. Multi-sourced, remote sensing data in levees monitoring: case study of SAFEDAM project. *The International Archives of the Photogrammetry, Remote Sensing and Spatial Information Sciences* 42. https://doi.org/10.5194/isprs-archives-XLII-3-W4-101-2018

Bakula, K., Pilarska, M., Salach, A., Kurczyński, Z., 2020. Detection of Levee Damage Based on UAS Data—Optical Imagery and LiDAR Point Clouds. *ISPRS International Journal of Geo-Information* 9, 248. https://doi.org/10.3390/ijgi9040248

Besl, P.J., McKay, N.D., 1992. A method for registration of 3-D shapes. *IEEE Transactions on Pattern Analysis and Machine Intelligence* 14, 239–256. https://doi.org/10.1109/34.121791

Brauneck, J., Pohl, R., Juepner, R., 2016. Experiences of using UAVs for monitoring levee breaches, in: *IOP Conference Series: Earth and Environmental Science.* IOP Publishing, p. 012046. https://doi.org/10.1088/1755-1315/46/1/012046

Dering, G.M., Micklethwaite, S., Thiele, S.T., Vollgger, S.A., Cruden, A.R., 2019. Review of drones, photogrammetry and emerging sensor technology for the study of dykes: Best practises and future potential. *Journal of Volcanology and Geothermal Research* 373, 148–166. https://doi.org/10.1016/j.jvolgeores.2019.01.018

Eltner, A., Kaiser, A., Castillo, C., Rock, G., Neugirg, F., Abellán, A., 2016a. Image-based surface reconstruction in geomorphometry–merits, limits and developments. *Earth Surface Dynamics* 4, 359–389. https://doi.org/10.5194/esurf-4-359-2016

Froideval, L., Pedoja, K., Garestier, F., Moulon, P., Conessa, C., Pellerin Le Bas, X., Traoré, K., Benoit, L., 2019. A low-cost open-source workflow to generate georeferenced 3D SfM photogrammetric models of rocky outcrops. *The Photogrammetric Record* 34, 365–384. https://doi.org/10.1111/phor.12297

Gienko, G.A., Terry, J.P., 2014. Three-dimensional modeling of coastal boulders using multi-view image measurements. *Earth surface processes and Landforms* 39, 853–864. https://doi.org/10.1002/esp.3485

Girardeau-Montaut, D., 2011.CloudCompare. 3D Point Cloud and Mesh Processing Software. OpenSource Project. http://www.danielgm.net/cc/ [Accessed: 10th December 2021].

Guillot, B., Pouget, F., 2015. UAV application in coastal environment, example of the Oleron island for dunes and dikes survey, in: *The International Archives of the Photogrammetry, Remote Sensing and Spatial Information Sciences,* ISPRS, Sep 2015, la grande motte, France. https://doi.org/10.5194/isprsarchives-XL-3-W3-321-2015

Hastaoğlu, K.Ö., Gül, Y., Poyraz, F., Kara, B.C., 2019. Monitoring 3D areal displacements by a new methodology and software using UAV photogrammetry. *International Journal of Applied Earth Observation and Geoinformation* 83, 101916. https://doi.org/10.1016/j.jag.2019.101916

Kaidi, S., Rouainia, M., Ouahsine, A., 2012. Stability of breakwaters under hydrodynamic loading using a coupled DDA/FEM approach. *Ocean Engineering*, 55, 62-70. https://doi.org/10.1016/j.oceaneng.2012.07.035

Lague, D., Brodu, N., Leroux, J., 2013. Accurate 3D comparison of complex topography with terrestrial laser scanner: Application to the Rangitikei canyon (NZ). *ISPRS journal of photogrammetry and remote sensing* 82, 10–26. https://doi.org/10.1016/j.isprsjprs.2013.04.009

Lowe, D.G., 2004. Distinctive image features from scale-invariant keypoints. *International journal of computer vision* 60, 91–110. https://doi.org/10.1023/ B:VISI.0000029664.99615. 94

Moulon, P., Monasse, P., Marlet, R., 2012. Adaptive structure from motion with a contrario model estimation, in: *Asian Conference on Computer Vision. Springer*, pp. 257–270. https://doi.org/10.1007/978-3-642-37447-0_20

Moulon, P., Monasse, P. and Marlet, R., 2016. OpenMVG (open Multiple View Geometry). https://github.com/openMVG / openMVG [Accessed: 10th December 2021].

Oats, R.C., Escobar-Wolf, R., Oommen, T., 2019. Evaluation of photogrammetry and inclusion of control points: Significance for infrastructure monitoring. *Data* 4, 42. https://doi.org/ 10.3390/data4010042

OpenMVS Development Team, 2018. CDC Sea Cave. https://github.com/cdcseacave/openMVS [Accessed: 10th December 2021].

Schnabel, R., Wahl, R., Klein, R., 2007. Efficient RANSAC for point-cloud shape detection, in: *Computer Graphics Forum.* Wiley Online Library, pp. 214–226. https://doi.org/10.1111/ j.1467-8659. 2007.01016.x

Tournadre, V., Pierrot-Deseilligny, M., Faure, P.-H., 2014. UAV photogrammetry to monitor dykes-calibration and comparison to terrestrial lidar. *The International Archives of Photogrammetry, Remote Sensing and Spatial Information Sciences* 40, 143. https://doi.org/10.5194/isprsarchives-XL-3-W1-143-2014

Zekkos, D., Greenwood, W., Lynch, J., Manousakis, J., Athanasopoulos-Zekkos, A., Clark, M., Cook, K., Saroglou, C., 2018. Lessons learned from the application of UAV-enabled structure-from-motion photogrammetry in geotechnical engineering. *Int. J. Geoeng. Case Hist*, 2018 vol. 4, no 4, p.254-274. https://dx.doi.org/10.4417/IJGCH-04-04-03

Zhou, Y., 2019. 100% automatic metrology with UAV photogrammetry and embedded GPS and its application in dike monitoring (*PhD Thesis*). Université Paris-Est. Bibcode: 2019PESC2033